Journal of the Taiwan Institute of Chemical Engineers 123 (2021) 228–244

Contents lists available at ScienceDirect

Journal of the Taiwan Institute of Chemical Engineers

journal homepage: www.elsevier.com/locate/jtice

$Bi_{12}SiO_{20}$/g-C_3N_4 heterojunctions: Synthesis, characterization, photocatalytic activity for organic pollutant degradation, and mechanism

Chiing-Chang Chen[a,*], Tsai-Ting Chen[a], Janah Shaya[b,c], Chan-Lun Wu[a], Chung-Shin Lu[d,*]

[a] Department of Science Education and Application, National Taichung University of Education, Taichung 403, Taiwan
[b] College of Medicine and Health Sciences, Khalifa University, P.O. Box 127788, Abu Dhabi, United Arab Emirates
[c] College of Arts and Sciences, Khalifa University, P.O. Box 127788, Abu Dhabi, United Arab Emirates
[d] Department of General Education, National Taichung University of Science and Technology, Taichung 403, Taiwan

ARTICLE INFO

Article History:
Received 10 March 2021
Revised 10 May 2021
Accepted 21 May 2021
Available online 10 June 2021

Keywords:
$Bi_{12}sio_{20}$
g-C_3N_4, Photocatalytic
Crystal violet
2-hydroxybenzoic acid

ABSTRACT

This work reports the synthesis of new and efficient composite photocatalysts ($Bi_{12}SiO_{20}$/g-C_3N_4) via the controlled hydrothermal method. The $Bi_{12}SiO_{20}$/g-C_3N_4 composites were characterized by XRD, SEM-EDS, HRTEM, FT-IR, XPS, DRS, BET, PL, and EPR. In comparison to pure $Bi_{12}SiO_{20}$ and g-C_3N_4, the $Bi_{12}SiO_{20}$/g-C_3N_4 materials showed significantly higher photocatalytic activity for degradation of crystal violet (CV) under visible-light irradiation (99% in 48 h). The 5 wt% $Bi_{12}SiO_{20}$/g-C_3N_4 composite revealed the highest rate constant of CV degradation (0.078 h^{-1}); 15 and 2 times larger than the constants obtained with individual $Bi_{12}SiO_{20}$ and g-C_3N_4, respectively. Further investigation of the photocatalytic activity of the 5 wt% $Bi_{12}SiO_{20}$/g-C_3N_4 materials were performed on other organic pollutants. 98% degradation of 2-hydroxybenzoic acid (2-HBA) and 99.5% degradation of rhodamine-B (RhB) were achieved upon exposure to visible-light irradiation for 72 h with 5 wt% $Bi_{12}SiO_{20}$/g-C_3N_4. $Bi_{12}SiO_{20}$/GO (graphene oxide) composites were also synthesized to compare the photocatalytic activities of different Bi heterojunctions. It was found that $Bi_{12}SiO_{20}$/g-C_3N_4 photocatalysts had enhanced photocatalytic activity in degradation of CV and 2-HBA and were considerably more stable in recycling experiments in comparison to $Bi_{12}SiO_{20}$/GO photocatalysts. Lastly, the plausible photocatalytic mechanism for the $Bi_{12}SiO_{20}$/g-C_3N_4 composite material was proposed and the principal active species involved in the photodegradation of CV were investigated using scavenger and ESR experiments. The $Bi_{12}SiO_{20}$/g-C_3N_4 composite demonstrates good photocatalytic activity, stability and reusability, demonstrating its prospective use in photodegradation applications under visible-light irradiation.

1. Introduction

Dyes and pigments represent an important category of compounds used in the development of numerous industry sectors. Triphenylmethane dyes (such as Crystal Violet (CV)), in particular, have found significant applications in food, cosmetics, paper, and leather industries [1]. A major cost of the use of such dyes is the serious environmental pollution they cause with an estimated amount of 10–15% discharge of dyestuffs into wastewater [2]. These dyes might alter the aquatic ecosystems by interfering with the penetration of light, and thus affecting the photosynthetic reactions in aquatic plants. In addition, these dyes pose serious hazards to aquatic organisms and to humans, since they are potential carcinogens, mutagens, and toxic compounds [3]. Different methods have been advanced for the removal of dyes such as biodegradation, membrane filtration, adsorption, coagulation, flocculation, and photocatalytic degradation [4]. Photocatalysis presents a set of benefits when compared to traditional technologies used in treatment of wastewater: fast oxidation kinetics, oxidation of contaminants with low concentrations, absence of polycyclic side products, and high efficiency [5–7]. In recent years, photocatalytic methods have been successfully used to degrade triphenylmethane dye contaminants. Crystal violet decomposition has been studied using several systems that produce active species, including TiO_2 [8], ZnO [9], Bi_2WO_6 [10], $BaTiO_3$ [11], and $Bi_xAg_yO_z$ [12]. Among various semiconductors, TiO_2 found significant uses because of its stability, high efficiency, and non-toxicity. Nonetheless, the fast rate of recombination of the photogenerated electron-hole pairs and the need for UV irradiation for TiO_2 activation still hinder the practical applications of TiO_2 [13]. Research is thus still focused on developing efficient visible-light-responsive photocatalysts and investigating their photocatalytic performance in various important applications.

Bismuth compounds, such as Bi_2O_3, BiOX (X = halogen), $Bi_2O_2CO_3$, $BiVO_4$, Bi_2SiO_5, and $Bi_{12}SiO_{20}$ have drawn great attention due to their high photocatalytic activity and excellent stability [14]. $Bi_{12}SiO_{20}$

* Corresponding authors.
E-mail addresses: ccchen@mail.ntcu.edu.tw (C.-C. Chen), cslu6@nutc.edu.tw (C.-S. Lu).

https://doi.org/10.1016/j.jtice.2021.05.042
1876-1070/

(BSO) is a member of Bi-containing oxide compounds with a body-centered cubic structure (space group I23), thus belonging to sillenite family. BSO exhibits a convenient bandgap energy (2.6 eV) and good photoconductivity, and is thus considered a prospective candidate for photocatalysis [15]. He and Gu reported the synthesis of BSO photocatalyst through chemical solution decomposition and its active role in photocatalytic degradation of Congo red, which was similar to the efficient activity of P25 TiO_2 [16]. Nevertheless, the high recombination rate of the photo-generated electrons and holes within single-component photocatalysis remains a limiting factor for applications. In that regard, chemical and morphological modifications of BSO are applied to reinforce the separation of photo-generated electron-hole pairs and to increase its surface area [17].

The unique properties of graphitic carbon nitride (g-C_3N_4) have received great research interest over the past years. g-C_3N_4 exhibits a narrow bandgap (2.7 eV), strong absorption of visible light, good chemical stability, nontoxicity, and excellent electrical properties [18]. Additionally, g-C_3N_4 can be readily prepared via thermal condensation of other commercially affordable nitrogen-rich reactants (e.g., urea, melamine, etc.) [19]. Consequently, g-C_3N_4-based materials present a potential candidate for several photocatalytic important processes like degradation of pollutants, CO_2 reduction, and water splitting, among others [20]. As shown in Table 1, different g-C_3N_4 composite materials have recently been reported with enhancement of photocatalytic activities for the degradation of crystal violet and improvement in charge carrier separations [21–29].

To the best of our knowledge, the synthesis of $Bi_{12}SiO_{20}$/g-C_3N_4 composites and their photocatalytic applications under visible-light irradiation have not been reported yet. Herein, $Bi_{12}SiO_{20}$/g-C_3N_4 composite photocatalysts were prepared via template-free hydrothermal synthesis and the materials were elaborately characterized via various techniques (XRD, SEM-EDS, HRTEM, FT-IR, XPS, DRS, and BET). The $Bi_{12}SiO_{20}$/g-C_3N_4 composites exhibited considerable improvement in photocatalytic degradation efficiency of crystal violet (CV) under visible-light irradiation, as compared to pure $Bi_{12}SiO_{20}$ and g-C_3N_4. In addition, The $Bi_{12}SiO_{20}$/g-C_3N_4 photocatalysts were efficiently tested in photodegradation of other organic pollutants (2-HBA and RhB). Lastly, the possible photocatalytic degradation mechanism and the involved reactive moieties in the degradation of the CV dye by the $Bi_{12}SiO_{20}$/g-C_3N_4 composite were studied and discussed.

2. Experimental

2.1. Materials

The chemical reagents were obtained from the respective suppliers and used without additional purification: bismuth nitrate, 5,5-Dimethyl-1-pyrroline *N*-oxide (DMPO), cetyltrimethylammonium bromide (CTAB), and sodium azide from Sigma-Aldrich; p-benzoquinone from Alfa Assar; CV dye from TCI; ammonium oxalate and sodium silicate from Osaka; 2-hydroxybenzoic acid and urea from Katayama; and isopropanol, sodium hydroxide, nitric acid (reagent-grade), ammonium acetate, and methanol (HPLC-grade) from Merck. Deionized water, purified using a Milli-Q water ion exchange system to obtain a resistivity of 1.8×10^7 Ω-cm, was always utilized in the experiments.

2.2. Apparatus and instruments

X-ray powder diffraction (XRD) was measured using a MAC Science MXP18 equipped with Cu-Ka radiation, operated at 80 mA and 40 kV. High-resolution transmission electron microscopy (HRTEM) images, selected area electron diffraction (SAED) patterns, and energy-dispersive X-ray spectra (EDS) were performed on a JEOL-2010 instrument (accelerating voltage = 200 kV). Field-emission scanning electron microscopy-electron dispersive X-ray spectroscopy (FE-SEM-EDS) was performed on a JEOL JSM-7401F instrument (accelerating voltage = 15 kV). 15 kV was used to generate the Al-Ka radiation. A ULVAC-PHI instrument was used for High-resolution X-ray photoelectron spectroscopy (HRXPS) and a ULVAC-PHI XPS, PHI Quantera SXM was utilized for Ultra-violet photoelectron spectroscopy (UPS). A Hitachi F-7000 instrument was used for Photoluminescence (PL) measurements. The Brunauer-Emmett-Teller (BET) specific surface areas were analyzed by a Micrometrics Gemini automated system utilizing nitrogen gas as the adsorbate at liquid nitrogen temperature.

2.3. Preparation and characterization of $Bi_{12}SiO_{20}$ /g-C_3N_4

The preparation of the g-C_3N_4 was carried out by calcination of melamine in a muffle furnace under atmospheric conditions. 5 g of melamine was transferred into an alumina crucible and heated to 540 °C for 4 h. 10 °C/min was used as the heating rate. The sample was then cooled to ambient temperature and put into an agate mortar for grinding. The obtained powder is graphitized carbon nitride (g-C_3N_4) photocatalyst. In parallel, 0.17 mmol of sodium silicate (Na_2SiO_3) and 2 mmol of bismuth nitrate ($Bi(NO_3)_3$•$5H_2O$) were dissolved in 10 mL of 3 M sodium hydroxide. After stirring for 30 min, the pH was adjusted to 13.3 by dropwise addition of 2 M NaOH. The mixture was placed in a 30 mL Teflon-lined autoclave and heated to 100 °C for 4 h. The obtained precipitate was collected by filtration, washed with deionized water several times, and then dried for 24 h at 60 °C. The sample was ground in an agate mortar, and the obtained powder is $Bi_{12}SiO_{20}$ photocatalyst. In solution A, 0.95 g of the prepared g-C_3N_4 was dissolved in 10 mL of ethylene glycol, and 0.05 g of cetyltrimethylammonium bromide (CTAB) was added and stirred for

Table 1
Degradation of the CV dye by graphitic carbon nitride composites under visible light irradiation.

Composite photocatalyst	g-C_3N_4(wt%)	Visible lamp	Catalyst dosage (gL^{-1})	Photocatalytic activity	Reference photocatalyst/ Enhancement factor	Reference
$SrFeO_{3-x}$/g-C_3N_4	96	150 W	0.1	95% decomposition in 24h	g-C_3N_4: 4.8	[21]
Ag_3VO_4/g-C_3N_4	40	500 W	1.0	75% decomposition in 2.5h	g-C_3N_4: 11.5 Ag_3VO_4: 6.6	[22]
$CaTiO_3$/g-C_3N_4	33.3	300 W	0.4	99.76% decomposition in 3h	g-C_3N_4: 2.5 $CaTiO_3$: 1.5	[23]
ZnO/g-C_3N_4	20	solar light	1.0	97% decomposition in 3h	g-C_3N_4: 1.4 ZnO: 1.4	[24]
SnO_2/g-C_3N_4	70	500 W	0.1	99% decomposition in 25min	g-C_3N_4: 5.06	[25]
Co-MOF/g-C_3N_4		MaX 303	0.2	95% decomposition in 80min	g-C_3N_4: 1.64 Co-MOF: 4.71	[26]
H-ZSM-5/g-C_3N_4	28	300 W	0.67	98% decomposition in 35min		[27]
$CaCO_3$/g—C_3N_4	3		1.0	76% decomposition in 3h	g-C_3N_4: 3.52	[28]
GA/g-C_3N_4	30	300 W	0.2	44.5% decomposition in 3h		[29]
$Bi_{12}SiO_{20}$/g-C_3N_4	5	150 W	0.1	99% decomposition in 48 h	g-C_3N_4: 2 $Bi_{12}SiO_{20}$: 15	This study

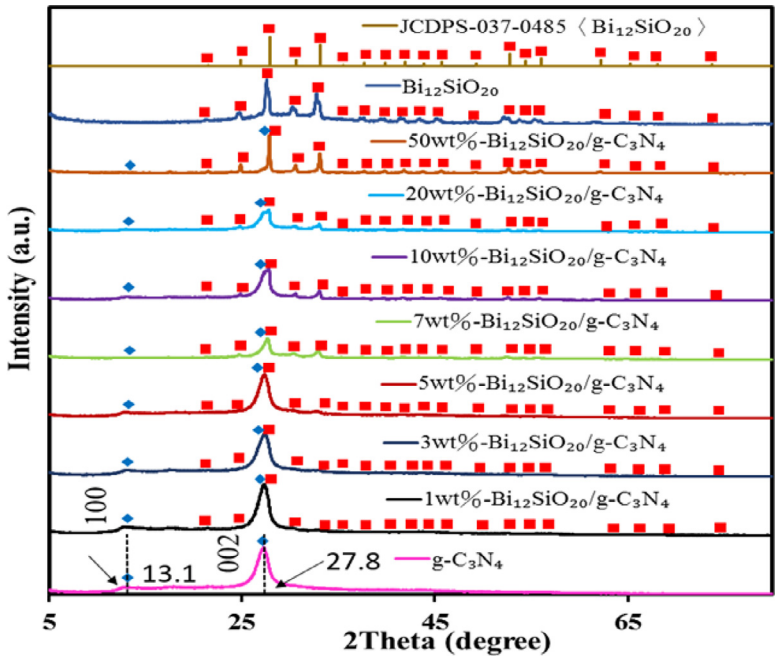

Fig. 1. XRD patterns of the as-prepared $Bi_{12}SiO_{20}$/g-C_3N_4 samples with different weight percentages (%).

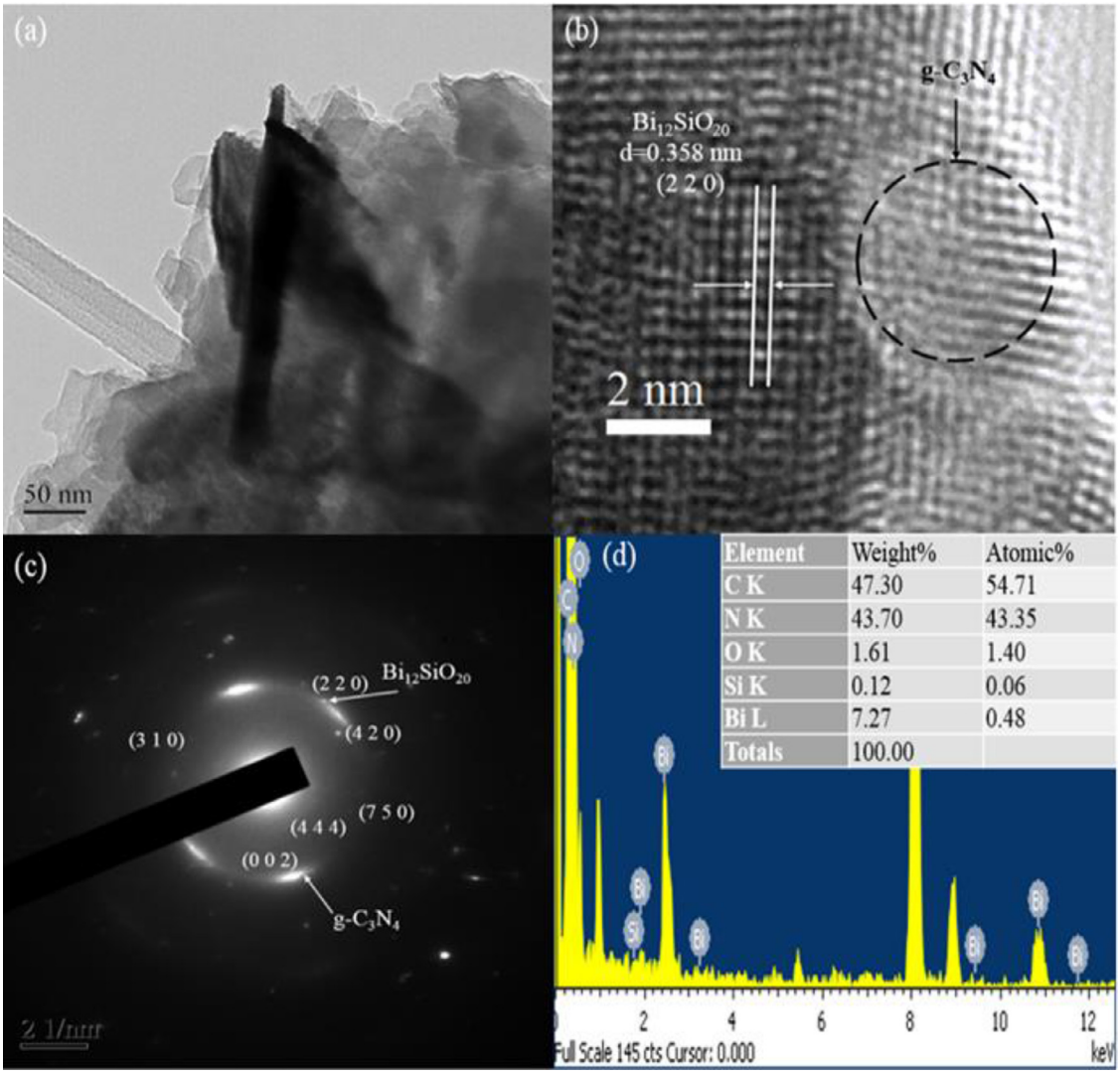

Fig. 2. FE-TEM and EDS of the as-prepared 5wt%-$Bi_{12}SiO_{20}$/g-C_3N_4 composite.

20 min. In solution B, 0.05 g of the prepared $Bi_{12}SiO_{20}$ was dissolved in 10 mL of ethylene glycol, and 0.07 g of urea was added and stirred for 20 min. The two solutions were then mixed and stirred for 40 min. The obtained mixture was placed in a 30 mL Teflon-lined autoclave and heated to 100 °C for 4 h. The obtained precipitate was filtered, washed with 500 mL alcohol solution (water:alcohol=3:2) and 2000 mL deionized water, and then dried for 24 h at 60 °C. The collected material was ground in an agate mortar, and the obtained powder is the $Bi_{12}SiO_{20}$/g-C_3N_4 composite photocatalyst.

2.4. Photocatalytic experiments

The photocatalytic activity of $Bi_{12}SiO_{20}$/g-C_3N_4 composites was assessed by degradation of CV dye (in addition to 2-HBA and RhB) under visible-light irradiation using 150 W Xe arc lamp. The reactor was fixed at a distance of 30 cm from the light source, and the light intensity was maintained at 31.2 W/m^2. In a typical run, 10 mg of the photocatalyst and the aqueous suspensions of CV, 2-HBA, or RhB (100 mL, 10 ppm) were added to the reaction vessel (Pyrex material). Then, HNO_3 or NaOH solution was used to adjust the pH of the suspension accordingly, and it was stirred about 30 min in the dark using a magnetic stirrer prior to irradiation to establish the adsorption/desorption equilibrium. 5 mL aliquots were collected at specific irradiation time intervals. The catalyst was removed from the aliquots by centrifugation. The residual CV dye (2-HBA, or RhB) was quantified in each cycle using HPLC-PDA-MS. The photocatalytic experiments were performed in duplicates to ensure reproducibility. Error bars represent the standard deviations of duplicate runs.

The roles of active species in this photocatalytic process were investigated using scavenger experiments to remove each species individually. Precisely, the following scavengers were added respectively: IPA (1.0 mM) for •OH; BQ (1.0 mM) for $•O_2^-$; AO (1.0 mM) for h^+; and lastly SA (1.0 mM) for $^1O_2$ [21]. The respective experimental procedures were similar to the abovementioned photocatalytic test.

3. Results and discussion

3.1. Characterization of $Bi_{12}SiO_{20}$/g-C_3N_4 composites

3.1.1. Phase structure

The XRD patterns of the $Bi_{12}SiO_{20}$/g-C_3N_4 composite samples are presented in Fig. 1. The patterns show that the prepared materials were well crystallized without impurities. Two peaks characteristic of g-C_3N_4 appear at 2Θ positions equal to 13.1° (100) and 27.8° (002). All prepared samples contain the $Bi_{12}SiO_{20}$ phase (JCPDS-00–037–0485) and the g-C_3N_4 phase (JCPDS 87–1526) [30–32]. The morphology of the 5wt%-$Bi_{12}SiO_{20}$/g-C_3N_4 samples recorded by transmission electron microscopy (TEM) is displayed in Fig. 2. The TEM image reveals the interfacial interaction between $Bi_{12}SiO_{20}$ and g-C_3N_4. The lattice spacing of 0.358 nm relevant to the (220) crystal plane of $Bi_{12}SiO_{20}$ and that of 0.326 nm associated to the (002) crystal plane of g-C_3N_4 are in close contact with each other [31,33]. Moreover, the EDS spectrum shows the existence of Bi, Si, O, C, and N elements. These results reveal the formation of the $Bi_{12}SiO_{20}$/g-C_3N_4 phase in the material, which is conducive to separation of photo-induced carriers and high photocatalytic activity.

Fig. 3 displays the FT-IR spectra for $Bi_{12}SiO_{20}$/g-C_3N_4 samples with different contents of $Bi_{12}SiO_{20}$. The absorption peaks located around 430 cm^{-1}, 570 cm^{-1}, and 860 cm^{-1} correspond to the stretching vibration modes of Bi–*O* bonds, SiO_4^{4-} groups, and Bi–*O*–Si bonds of $Bi_{12}SiO_{20}$, respectively [34]. The absorption peak at 812 cm^{-1} is

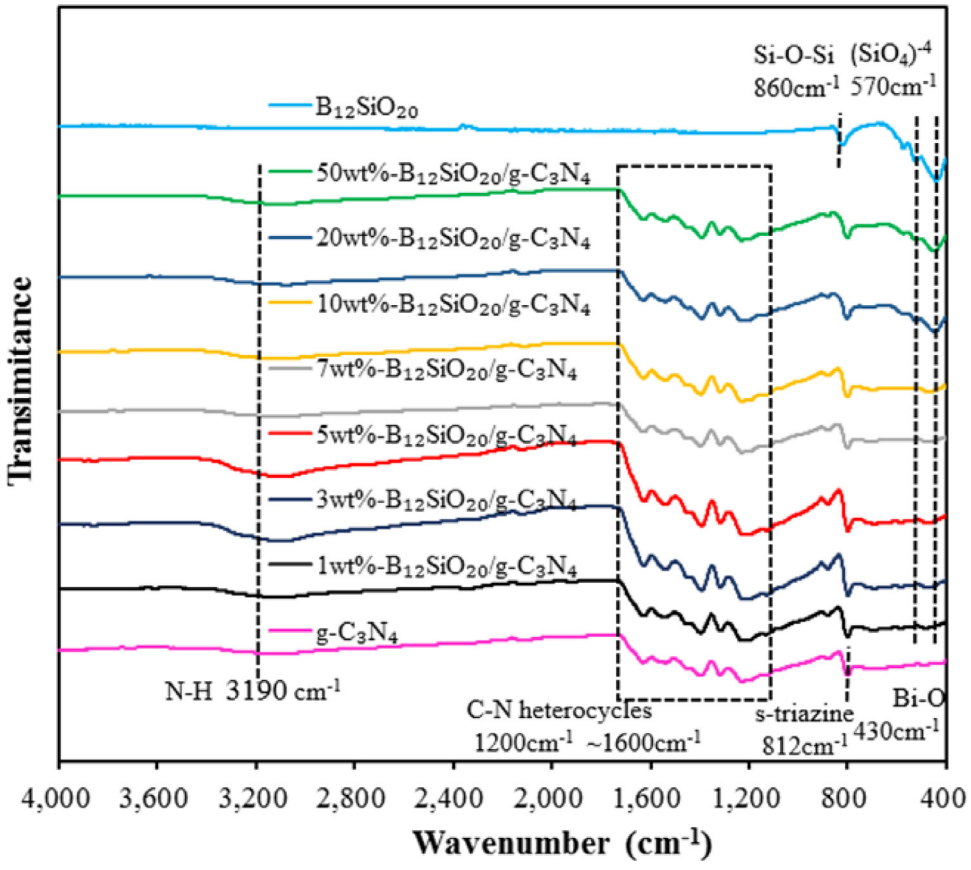

Fig. 3. FTIR spectra of the as-prepared $Bi_{12}SiO_{20}$/g-C_3N_4 samples with different weight percentages (%).

attributed to the characteristic breathing mode of s-triazine, and those at 1241, 1319, 1409, 1569, and 1642 cm^{-1} are related to the stretching modes of *C–N* heterocycles in g-C_3N_4 [35]. The characteristic peaks of $Bi_{12}SiO_{20}$ in the $Bi_{12}SiO_{20}$/g-C_3N_4 composites became more distinct as the $Bi_{12}SiO_{20}$ content increased, in agreement with the XRD patterns.

$Bi_{12}SiO_{20}$/g-C_3N_4 composites can be formed as proposed in Eqs. (1 – 5) . The experimental results infer that compounds synthesized under different hydrothermal conditions have undergone the following series of changes: $Bi_2Si_3O_9$ →$Bi_4Si_3O_{12}$ →Bi_2SiO_5 →$Bi_{12}SiO_{20}$. Different composition of bismuth silicates can be prepared as described in the equations below, which are specific according to the pH control of the hydrothermal synthesis [34].

$$2Bi^{3+} + 3SiO_3^{2-} \rightarrow Bi_2Si_3O_{9(s)} \quad (1)$$

$$2Bi_2Si_3O_{9(s)} + 6OH^- \rightarrow Bi_4Si_3O_{12(s)} + 3SiO_3^{2-} + 3H_2O \quad (2)$$

$$Bi_4Si_3O_{12(s)} + 2OH^- \rightarrow 2Bi_2SiO_{5(s)} + SiO_3^{2-} + H_2O \quad (3)$$

$$6Bi_2SiO_{5(s)} + 10OH^- \rightarrow Bi_{12}SiO_{20(s)} + 5SiO_3^{2-} + 5H_2O \quad (4)$$

$$Bi_{12}SiO_{20(s)} + g - C_3N_4 \rightarrow Bi_{12}SiO_{20}/g - C_3N_{4(s)} \quad (5)$$

3.1.2. X-ray photoelectron spectroscopy

Fig. 4 shows the XPS spectra of the g-C_3N_4, $Bi_{12}SiO_{20}$, and 5wt%-$Bi_{12}SiO_{20}$/g-C_3N_4 samples. The survey scan XPS spectra (Fig. 4a) show a consistent chemical composition of the prepared materials;

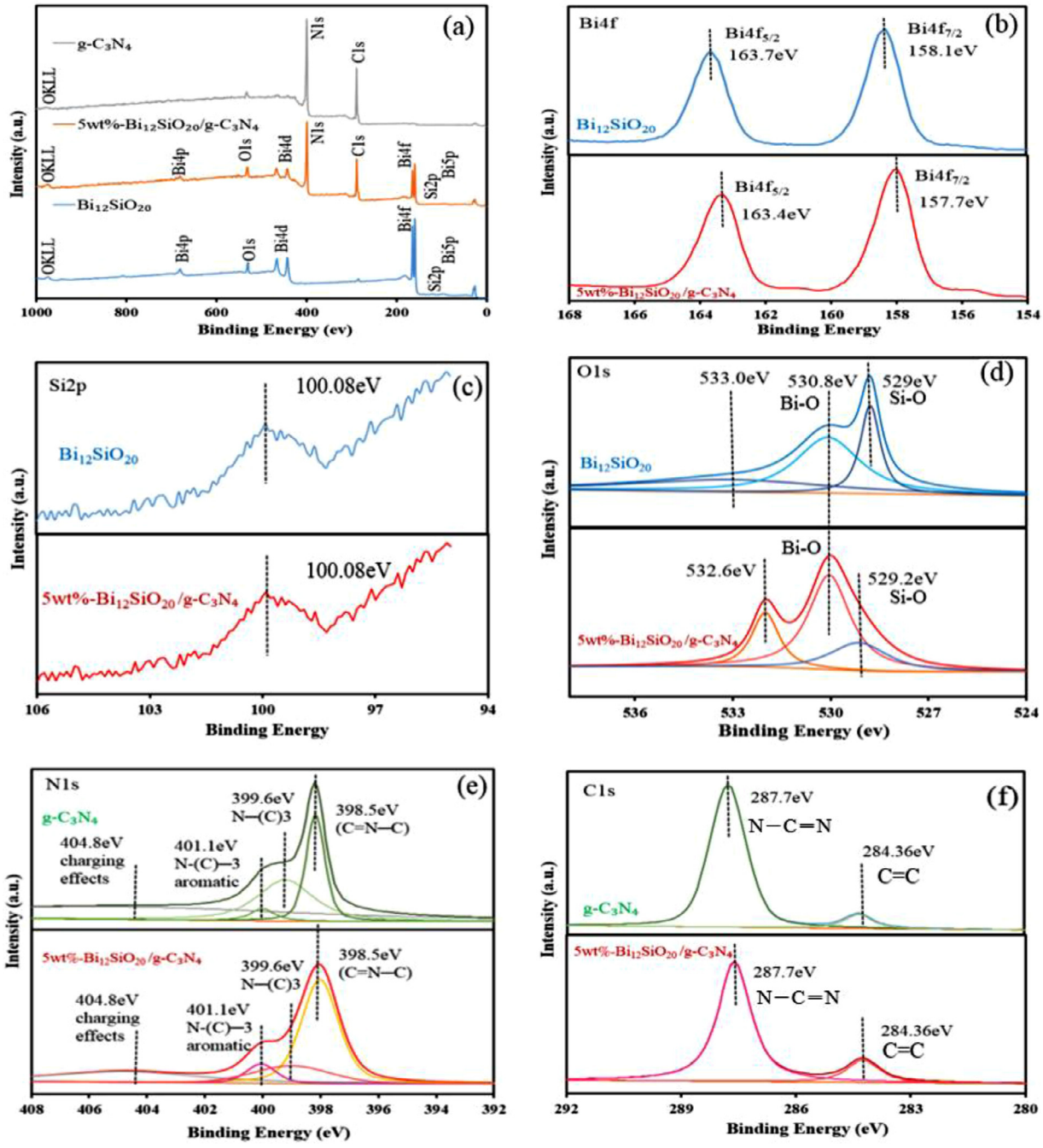

Fig. 4. High resolution XPS spectra of the $Bi_{12}SiO_{20}$, g-C_3N_4 and 5wt%-$Bi_{12}SiO_{20}$/g-C_3N_4 composite: (a) total survey, (b) Bi 4f, (c) Si 2p, (d) O 1 s, (e) N 1 s, and (f) C 1 s.

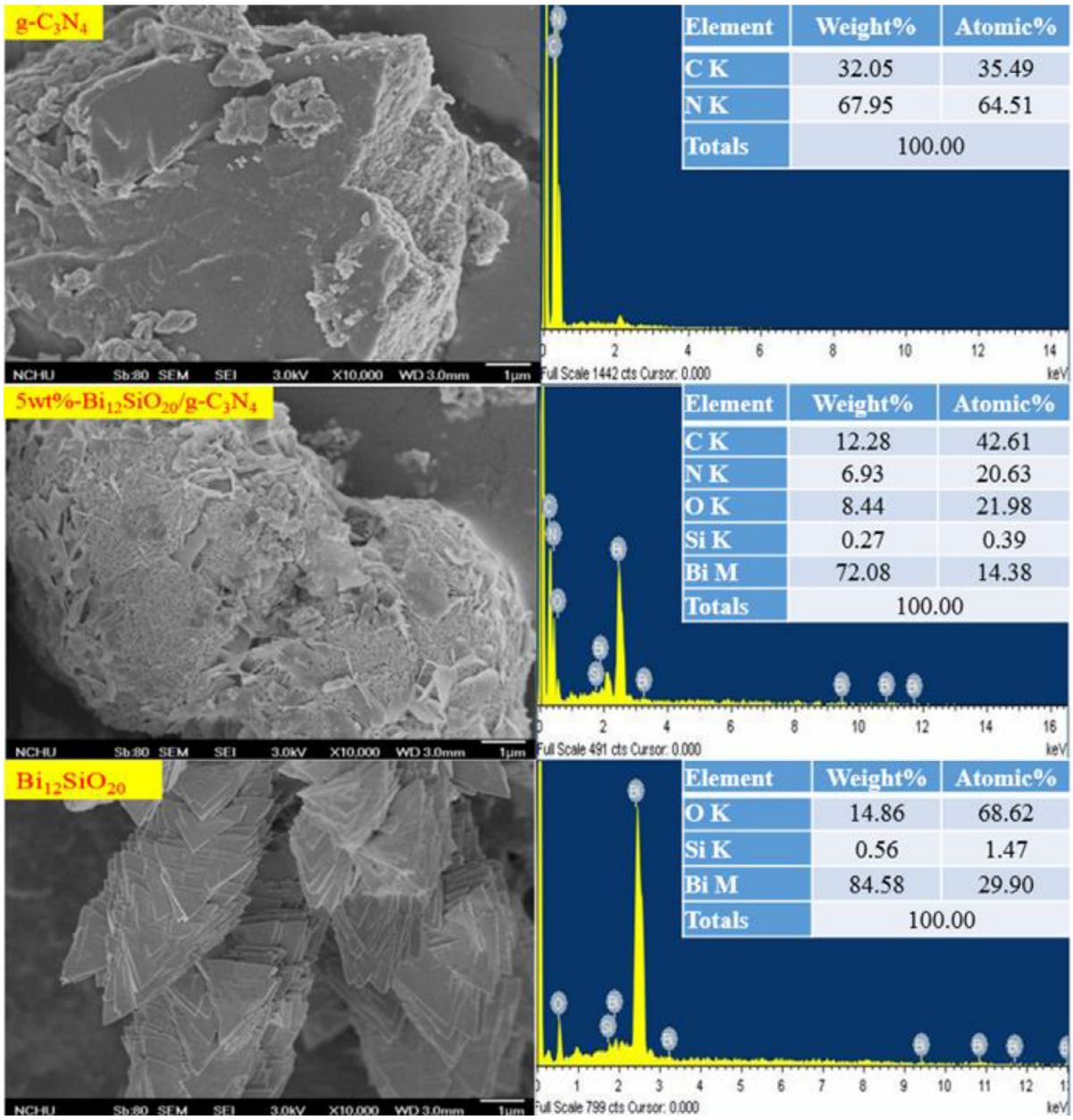

Fig. 5. FE-SEM and EDS of the as-prepared $Bi_{12}SiO_{20}$, g-C_3N_4, and 5wt%-$Bi_{12}SiO_{20}$/g-C_3N_4.

precisely C-1 s and N-1 s peaks of g-C_3N_4 as well as Bi-4f, Si-2p, and O-1 s peaks for $Bi_{12}SiO_{20}$ and all the respective peaks for the composite sample. The spectra in Fig. 4b display two symmetrical peaks for the Bi materials binding energies of 163.7 and 158.1 eV for $Bi_{12}SiO_{20}$, and 163.4 eV and 157.7 eV for 5wt%-$Bi_{12}SiO_{20}$/g-C_3N_4. These patterns represent the characteristic peaks of the respective spin-orbit splitting of Bi-4$f_{5/2}$ and Bi-4$f_{7/2}$; conforming to Bi^{+3} ion [36]. Fig. 4c shows the binding energy of Si 2$p_{3/2}$ located at 100.8 eV, which infers a tetravalent oxidation state of Si [34]. The asymmetry in the O-1 s spectra (Fig. 4d) can be split to result 3 different peaks at 529.0, 530.8, and 533.0 eV by the XPS peak-fitting program, respectively corresponding to Si–O, Bi–O, and surface hydroxyl groups (or adsorbed H_2O) binding energies [15]. The N-1 s spectra (Fig. 4e) show splitting into three peaks at 398.5, 399.6, and 401.1 eV. The first one corresponds to the sp^2-hybridized N in triazine rings (*C*–*N*=C), the second is ascribed to tertiary N in N-$(C)_3$ moieties, and the last to amino functional groups in C–N–H pattern. Another small peak is observed at 404.8 eV, and it is related to positive charge localization or charging effects in the heterocycles [37,38]. Lastly, Fig. 4f presents the C-1 s spectra with two peaks at 284.6 eV, from external hydrocarbon in the instrument, and characteristic 287.7 eV. The latter infers the presence of g-C_3N_4 as a characteristic peak of the sp^2-bonded carbon (N–*C*=*N*) [39,40].

Table 2
Composition and characterization of $Bi_{12}SiO_{20}$/g-C_3N_4 samples.

	EDS of atomic ratio(%)					Eg
Catalyst code	C	N	Bi	Si	O	
g-C_3N_4	35.49	65.51	–	–	–	2.50 eV
1wt%-$Bi_{12}SiO_{20}$/g-C_3N_4	36.84	61.21	0.04	0.04	1.87	2.60 eV
3wt%-$Bi_{12}SiO_{20}$/g-C_3N_4	35.71	58.46	0.39	0.02	5.41	2.45 eV
5wt%-$Bi_{12}SiO_{20}$/g-C_3N_4	42.64	20.63	14.38	0.39	21.98	2.36 eV
7wt%-$Bi_{12}SiO_{20}$/g-C_3N_4	35.71	58.46	0.39	0.02	5.41	2.52 eV
10wt%-$Bi_{12}SiO_{20}$/g-C_3N_4	35.14	57.39	1.03	0.15	6.29	2.51 eV
20wt%-$Bi_{12}SiO_{20}$/g-C_3N_4	37.53	57.91	0.24	0.14	4.17	2.56 eV
50wt%-$Bi_{12}SiO_{20}$/g-C_3N_4	42.61	20.63	14.38	0.39	21.98	2.41 eV
$Bi_{12}SiO_{20}$	–	–	68.62	1.47	29.90	2.38 eV

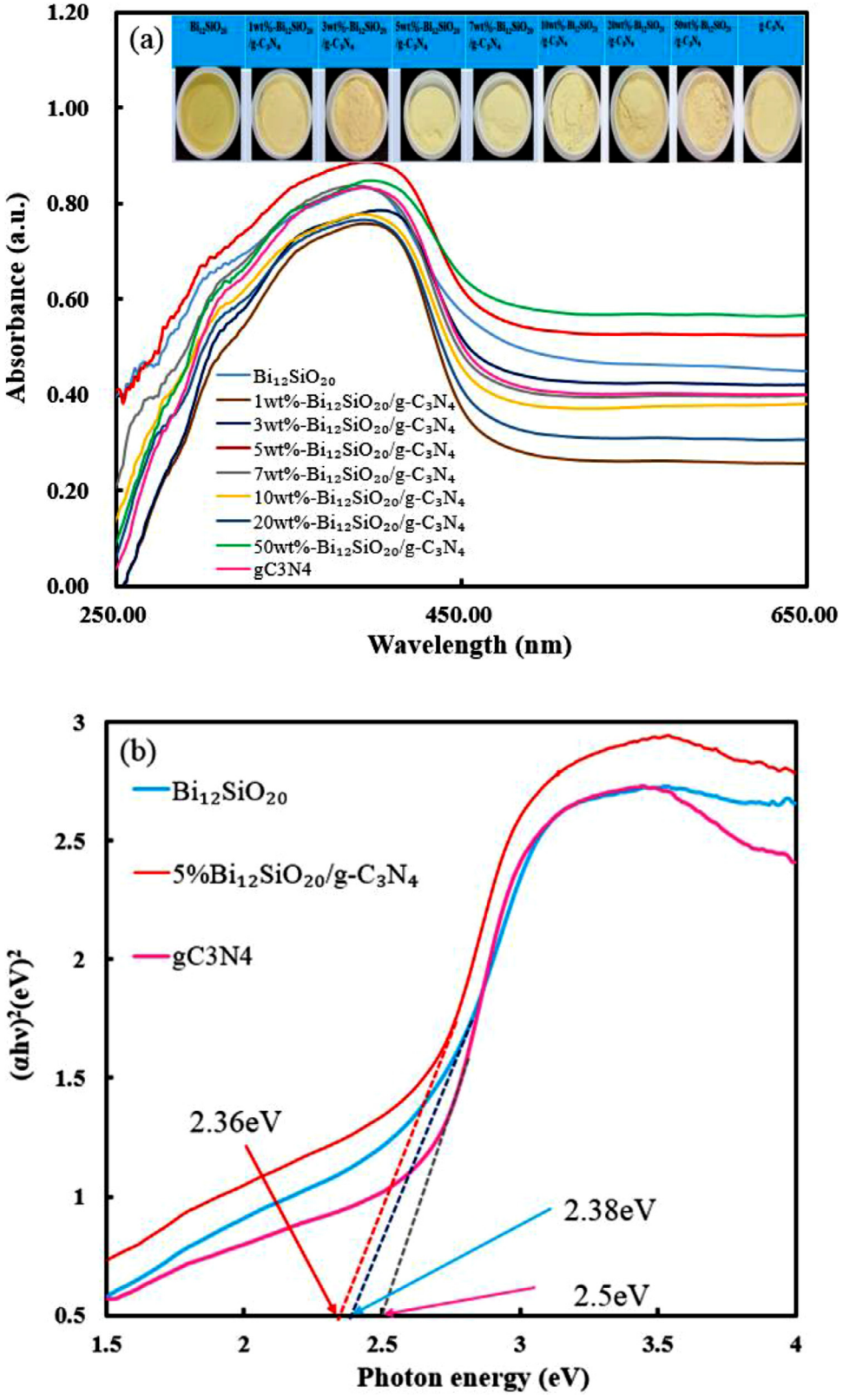

Fig. 6. DRS patterns of the as-prepared $Bi_{12}SiO_{20}$, g-C_3N_4, and 5wt%-$Bi_{12}SiO_{20}$/g-C_3N_4.

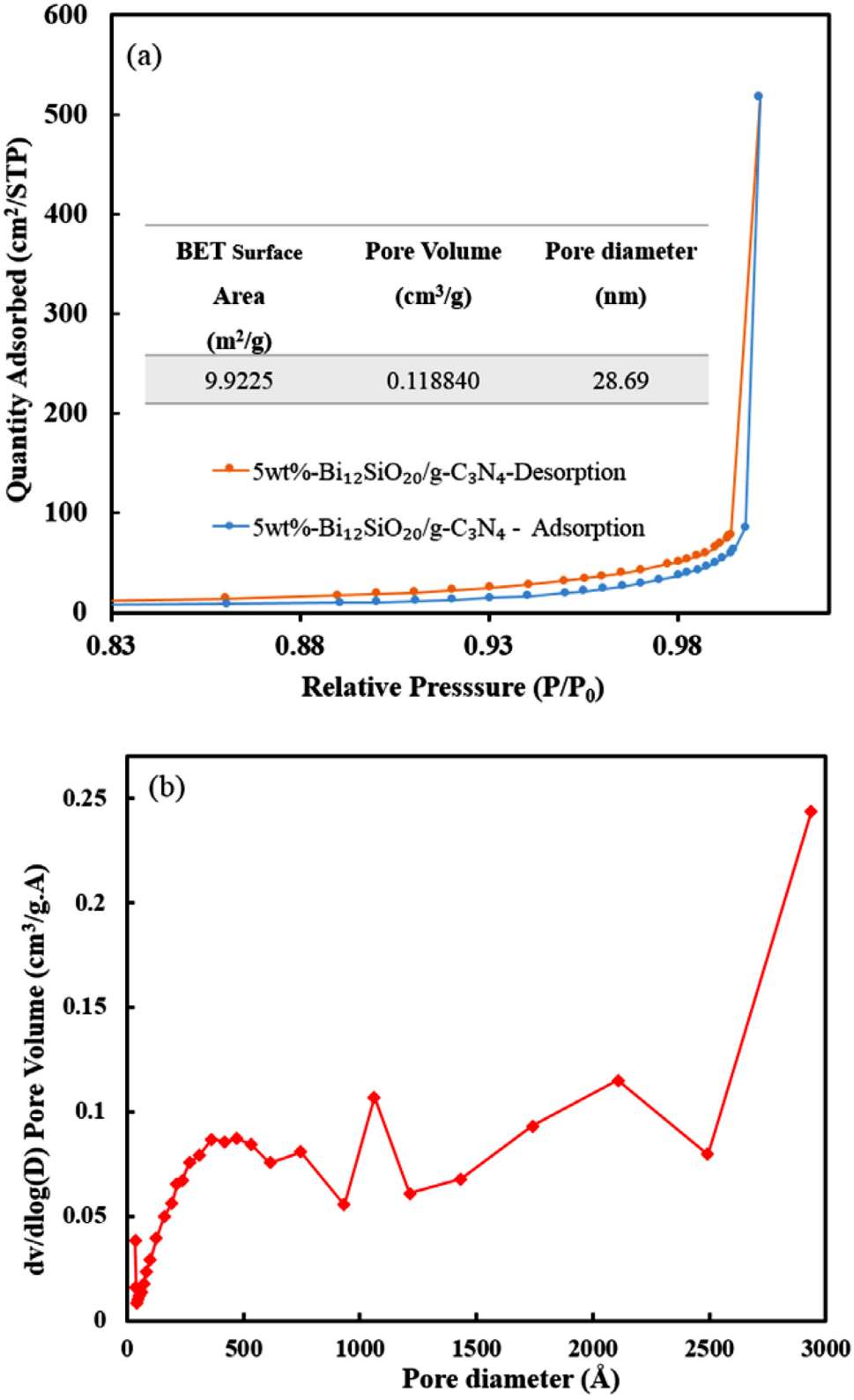

Fig. 7. N_2 adsorption–desorption isotherms and pore size distribution of 5wt%-$Bi_{12}SiO_{20}$/g-C_3N_4.

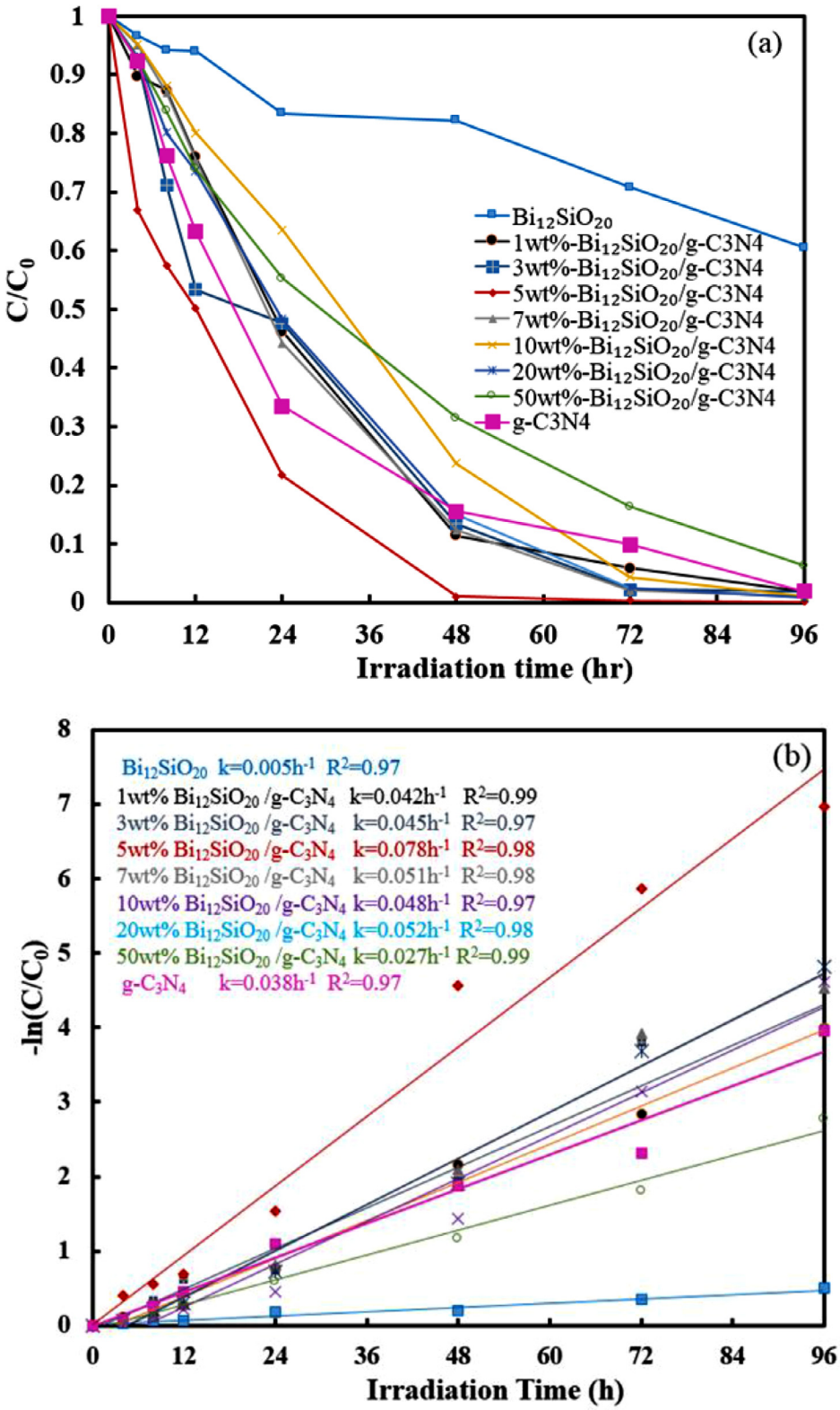

Fig. 8. Photodegradation of CV, 2-HBA and RhB as a function of irradiation time, using the as-prepared $Bi_{12}SiO_{20}$, g-C_3N_4, and 5wt%-$Bi_{12}SiO_{20}$/g-C_3N_4.

Table 3
Kinetic parameters (rate constants and linear regression coefficients R^2) for photocatalytic degradation of CV at various $Bi_{12}SiO_{20}$/g-C_3N_4 samples.

Sample	K(h^{-1})	R^2
$Bi_{12}SiO_{20}$	0.005	0.97
1wt% $Bi_{12}SiO_{20}$/g-C_3N_4	0.042	0.99
3wt% $Bi_{12}SiO_{20}$/g-C_3N_4	0.045	0.97
5wt% $Bi_{12}SiO_{20}$/g-C_3N_4	0.078	0.98
7wt% $Bi_{12}SiO_{20}$/g-C_3N_4	0.051	0.98
10wt% $Bi_{12}SiO_{20}$/g-C_3N_4	0.048	0.97
20wt% $Bi_{12}SiO_{20}$/g-C_3N_4	0.052	0.98
50wt% $Bi_{12}SiO_{20}$/g-C_3N_4	0.027	0.98
g-C_3N_4	0.038	0.97

Altogether, these spectra confirm the presence of graphite-like carbon nitride in the prepared materials.

3.1.3. Morphological structure and composition

The morphologies of the as-prepared pure g-C_3N_4, pristine $Bi_{12}SiO_{20}$, and 5wt%-$Bi_{12}SiO_{20}$/g-C_3N_4 samples were investigated using FE-SEM. g-C_3N_4 demonstrated a stacking layer-like structure (Fig. 5a), in agreement with the literature [41]. $Bi_{12}SiO_{20}$ sample appeared as a stacked-triangle-plate structure (Fig. 5b). This special morphology allows to easily identify the $Bi_{12}SiO_{20}$ in the SEM image of the $Bi_{12}SiO_{20}$/g-C_3N_4 composites. Fig. 5c displays the formation of the composite structure and the deposition of the plate-like $Bi_{12}SiO_{20}$ on the surface of g-C_3N_4. In line, the SEM-EDS results affirm the coexistence of $Bi_{12}SiO_{20}$ and g-C_3N_4 and the presence of C, N, O, Si, and Bi in the composite material (Table 2).

3.1.4. Optical absorption properties

The UV–Vis diffuse reflectance spectra of the different materials are depicted in Fig. 6a. The absorption edges of $Bi_{12}SiO_{20}$ appeared around 521 nm and that of g-C_3N_4 was positioned around 496 nm. These peaks conform to the pale-yellow appearance of the samples. The absorption band displayed in the $Bi_{12}SiO_{20}$/g-C_3N_4 spectra resembles the ones appearing in pure g-C_3N_4. Thus, introducing $Bi_{12}SiO_{20}$ into g-C_3N_4 had very small impact on optical properties. The bandgap energies of $Bi_{12}SiO_{20}$, g-C_3N_4, and 5wt%-$Bi_{12}SiO_{20}$/g-C_3N_4 are estimated to be about 2.38, 2.5, and 2.36 eV, respectively, according to plots of $(ahv)^2$ as a function of the photon energy (hv) (Fig. 6b) [42]. The DRS results indicate that the photocatalysts should possess visible-light photocatalytic activity.

3.1.5. BET and adsorption-desorption isotherm

Fig. 7 displays the nitrogen adsorption-desorption isotherm of 5wt%-$Bi_{12}SiO_{20}$/g-C_3N_4. The samples exhibit a type-IV isotherm, which suggests that they are mesoporous materials [43]. It can also be observed that the hysteresis loop belongs to type H3, which suggests the existence of slit-shaped pores that result from the aggregation of plate-like particles in general [44]. The specific surface areas of g-C_3N_4 and $Bi_{12}SiO_{20}$ were 17.60 and 0.27 m^2/g, respectively. The specific surface area declined from 17.60 (g-C_3N_4) to 9.92 m^2/g (5wt%-$Bi_{12}SiO_{20}$/g-C_3N_4) upon loading the $Bi_{12}SiO_{20}$ particles on the g-C_3N_4. This can be due to the partial clogging of the surface and pores of the g-C_3N_4 by the $Bi_{12}SiO_{20}$ particles. Lastly, the specific surface area of 5wt%-$Bi_{12}SiO_{20}$/g-C_3N_4 is much larger than that of the pure $Bi_{12}SiO_{20}$. This is because g-C_3N_4 restricts the aggregation of the $Bi_{12}SiO_{20}$ particles in the composite sample [35].

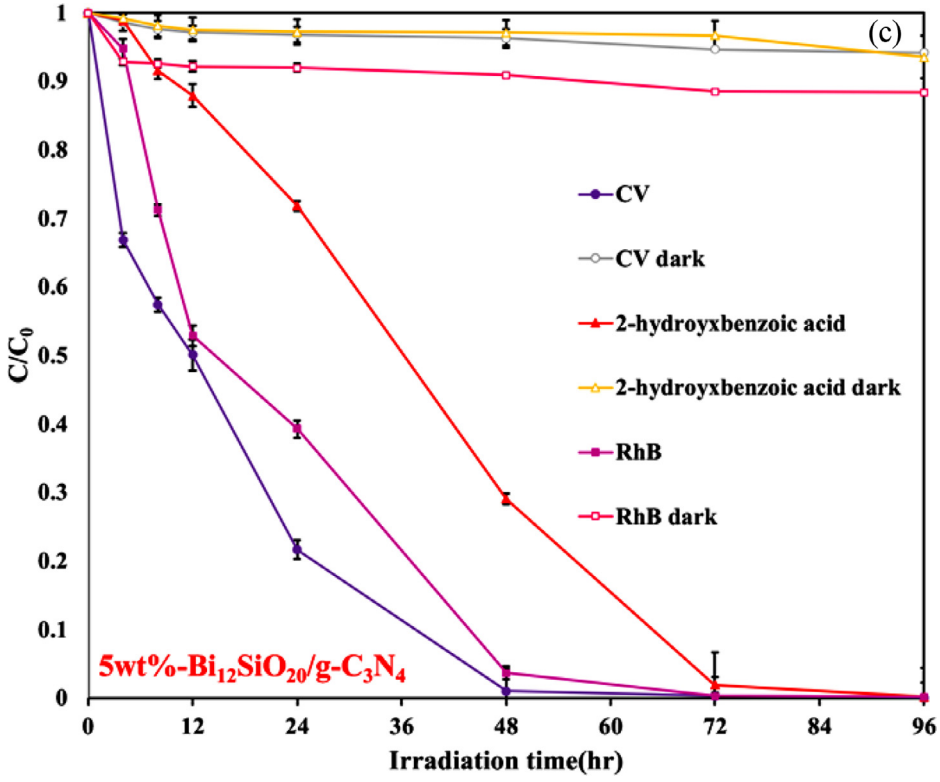

Fig. 8. Continued.

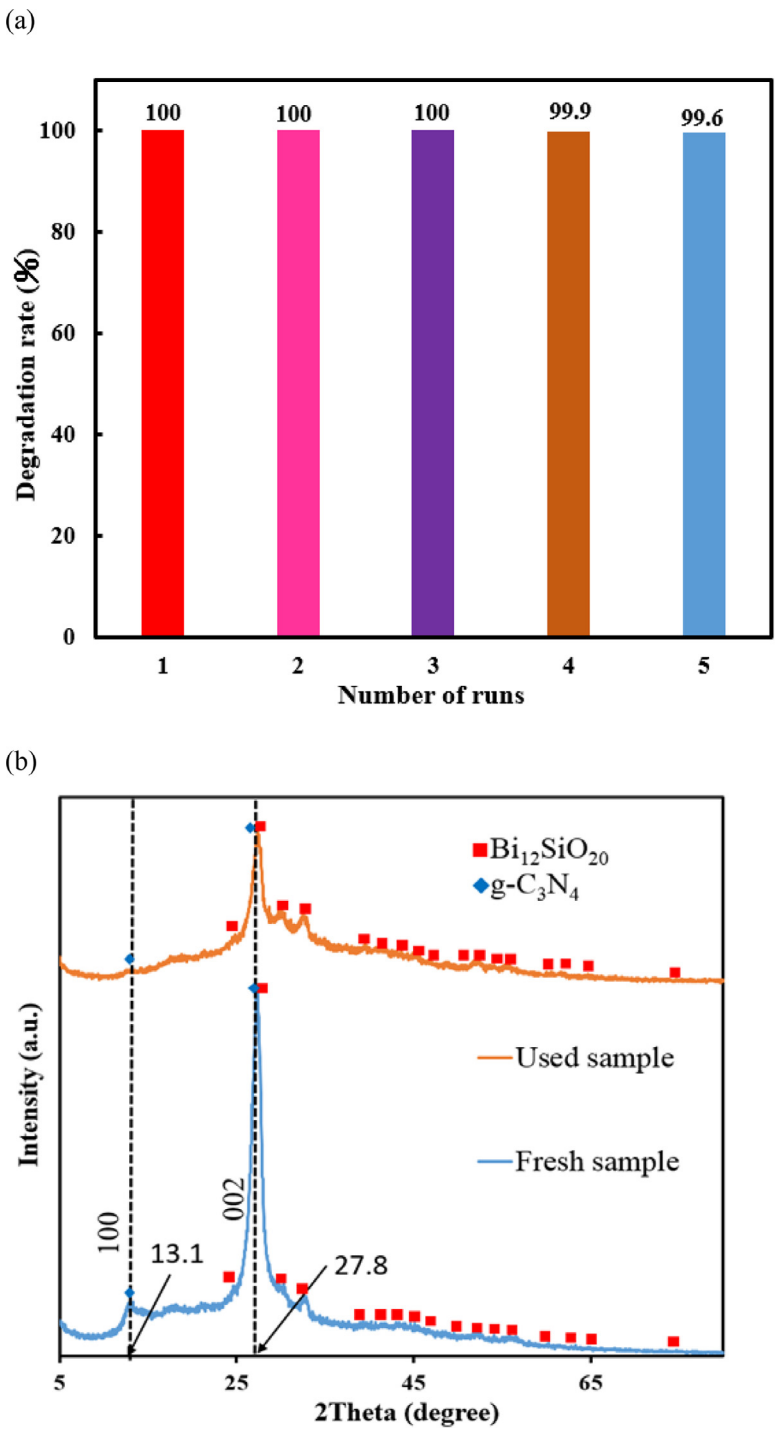

Fig. 9. (a) Cycling runs in the photocatalytic degradation of CV in the presence of 5wt%-$Bi_{12}SiO_{20}$/g-C_3N_4, (b) XRD of the sample powder before and after the degradation reaction, (c) SEM images of the sample powder before and after the degradation reaction.

3.2. *Photocatalytic activity of $Bi_{12}SiO_{20}$/g-C_3N_4 composites*

To study the photocatalytic activities of $Bi_{12}SiO_{20}$/g-C_3N_4 composites, CV dye was used and the photodegradation investigation was performed using visible-light irradiation. Fig. 8a presents the variation of the CV degradation rates on the catalysts with the irradiation time. The best photocatalytic activity among all catalysts was observed with the 5wt%-$Bi_{12}SiO_{20}$/g-C_3N_4 sample, achieving a CV degradation of 99% after 48 h of visible-light irradiation. The reaction kinetics of the CV degradation process was investigated more using the plots of ln(Co/C) as a function of visible-light irradiation time (hr) and by calculating the rate constants of the reactions. The CV photodegradation reaction over these catalysts was found to fit the pseudo-first-order kinetics equation ln(Co/C) = kt (Fig. 8b) [45]. Table 3 summarizes the rate constants of the different tested samples. The degradation rate constant over 5wt%-$Bi_{12}SiO_{20}$/g-C_3N_4 is

(c)

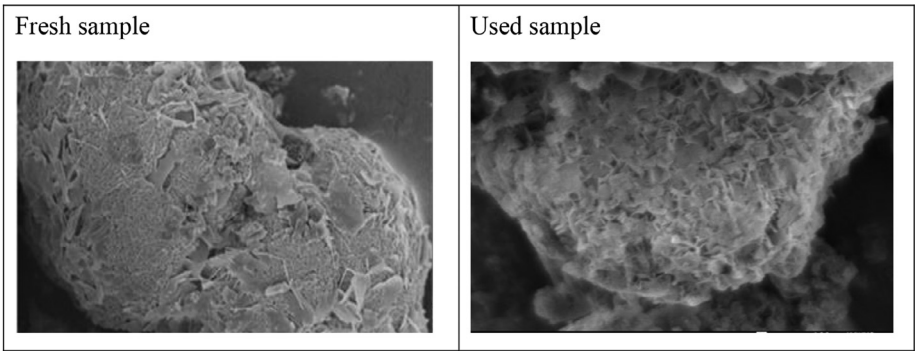

Fig. 9. Continued.

7.8×10^{-2} h^{-1}, which is 15 and 2 times more than the constants obtained over the $Bi_{12}SiO_{20}$ and g-C_3N_4, respectively. 2-hydroxybenzoic acid (2-HBA) and rhodamine B (RhB) were also used as target pollutants to further investigate the photocatalytic performance of 5wt%-$Bi_{12}SiO_{20}$/g-C_3N_4. About 98% of 2-HBA and 99.5% of RhB were photodegraded upon exposure to visible-light irradiation for 72 h, respectively (Fig. 8c). This further attests for the important photocatalytic activity of 5wt%-$Bi_{12}SiO_{20}$/g-C_3N_4, in line with the results achieved in degrading the CV dye.

The durability of the 5wt%-$Bi_{12}SiO_{20}$/g-C_3N_4 composite was tested during five consecutive CV photodegradation cycles. The photocatalyst was collected by centrifugation after each cycle and reused in the next run. As shown in Fig. 9a, the photocatalyst retained its high catalytic activity for 5 successive runs. Moreover, the XRD patterns of the reused 5wt%-$Bi_{12}SiO_{20}$/g-C_3N_4 composite remained in close match with those of the fresh powder, with only a small difference in their relative intensities (Fig. 9b). Lastly, the morphology of the 5wt%-$Bi_{12}SiO_{20}$/g-C_3N_4 was compared before and after the reactions using SEM images, showing no significant change after five reaction cycles (Fig. 9c). These experiments demonstrate the photostability of the 5wt%-$Bi_{12}SiO_{20}$/g-C_3N_4 composite.

Photoluminescence emission arises from the recombination of the free charge carriers, and a lower emission intensity generally reflects a lower electron-hole recombination rate, and consequently a more efficient photocatalytic activity. PL emission spectra were thus recorded to understand the photogenerated processes in the prepared semiconductors [41,45]. The spectra of the $Bi_{12}SiO_{20}$/g-C_3N_4 composites are depicted in Fig. 10. Among all samples, 5wt%-$Bi_{12}SiO_{20}$/g-C_3N_4 had the lowest PL intensity. This result confirms that the efficient transfer of photoinduced electrons between $Bi_{12}SiO_{20}$ and g-C_3N_4 enhances the ability of this composite to separate the photoinduced electron-hole pair, consequently increasing the photocatalytic activity in line with our previous results.

3.3. Characterization and photocatalytic activity of other $Bi_{12}SiO_{20}$ composites ($Bi_{12}SiO_{20}$/GO)

In order to compare the catalytic activity of $Bi_{12}SiO_{20}$/g-C_3N_4 composites to other Bi composite materials, $Bi_{12}SiO_{20}$/GO (graphene

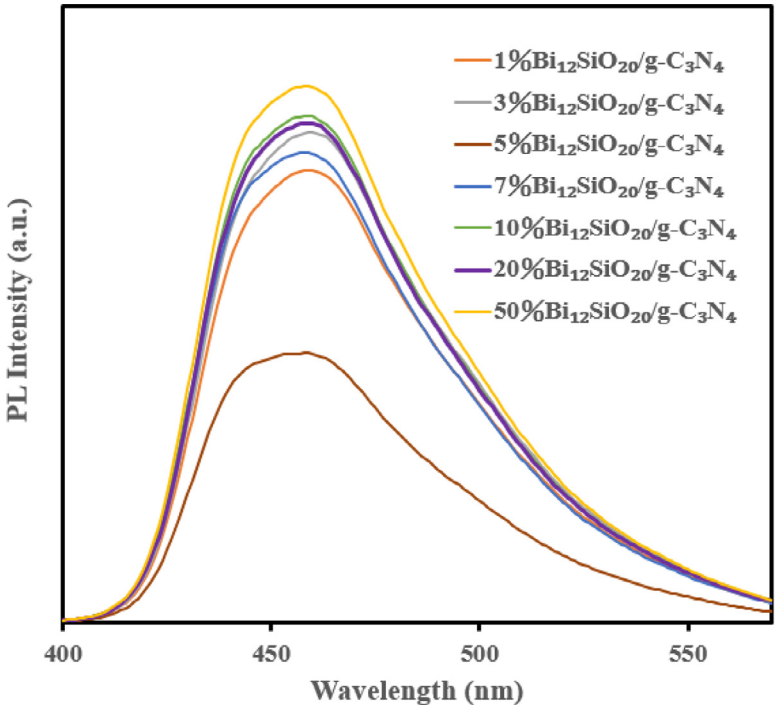

Fig. 10. PL spectra of the as-prepared $Bi_{12}SiO_{20}$/g-C_3N_4 samples with different weight percentages (%).

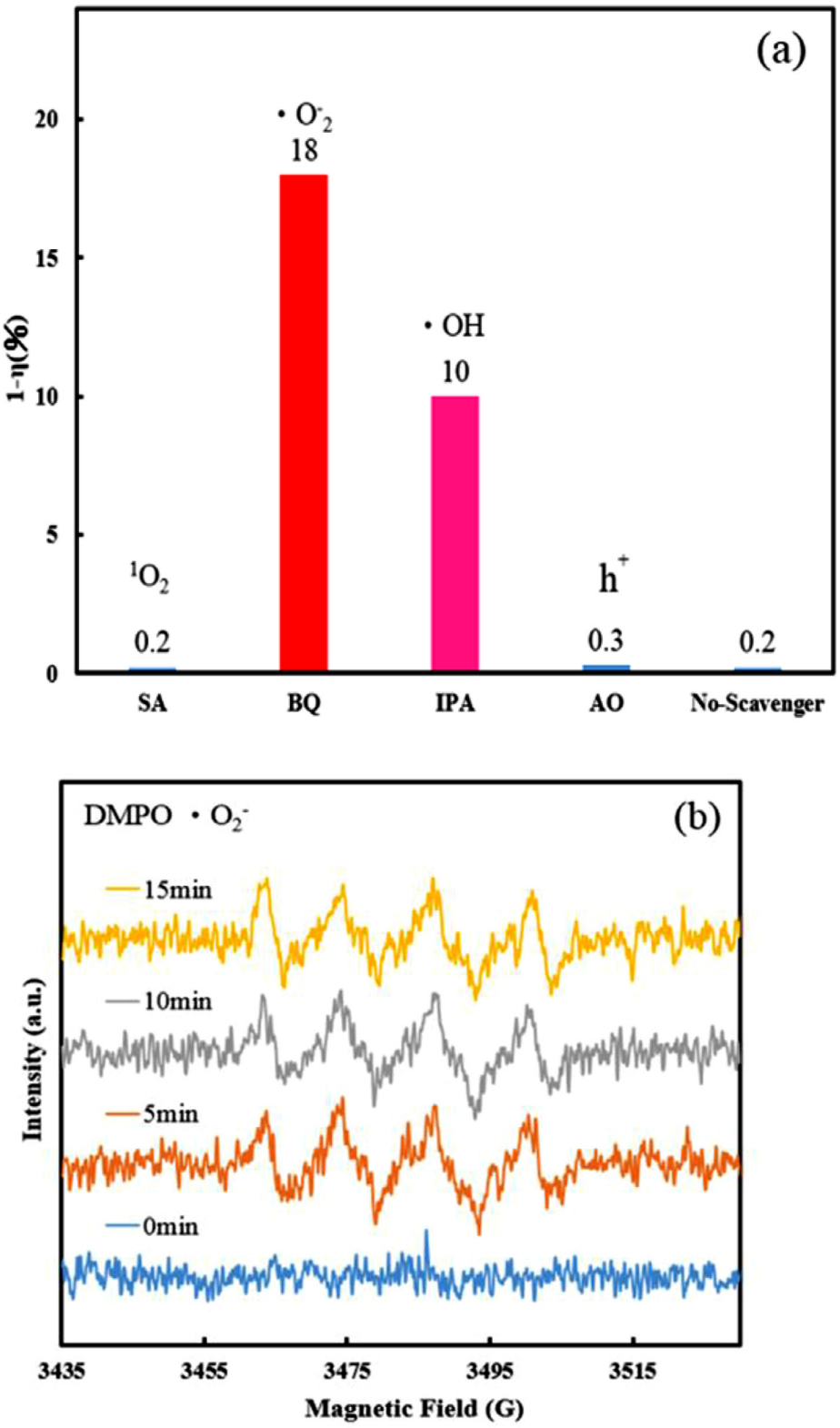

Fig. 11. (a) Trapping of active species during the photocatalytic reaction using 5wt%-$Bi_{12}SiO_{20}$/g-C_3N_4, (b) and (c) ESR spectra of DMPO-•O_2^- and DMPO-•OH using 5wt%-$Bi_{12}SiO_{20}$/g-C_3N_4 dispersion in methanol solution under visible light irradiation.

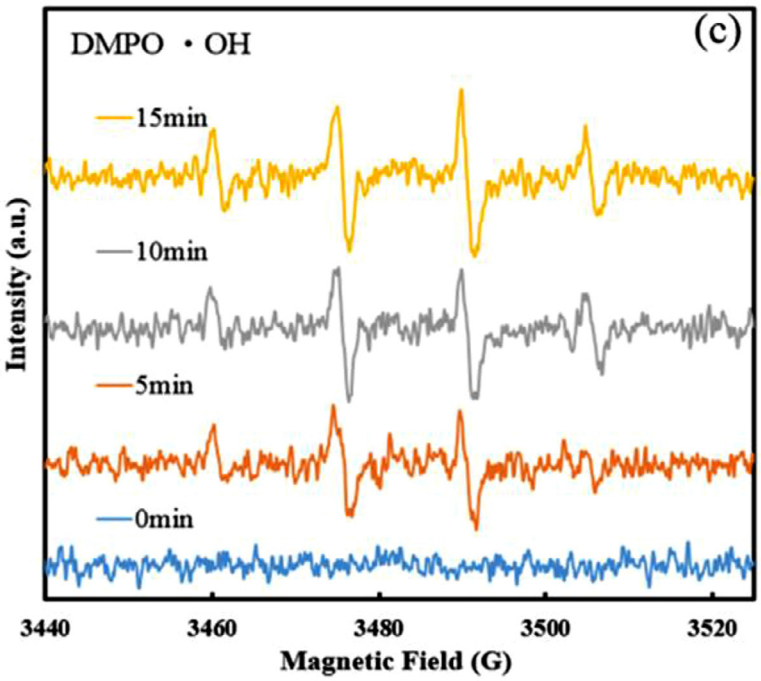

Fig. 11. Continued.

oxide) composites were also prepared with varied GO contents via a simple hydrothermal method. The synthetic procedure and the characterization of the prepared composites (XRD, TEM, FTIR, XPS, SEM–EDS, BET, and UV–vis DRS) are described in the supplementary materials (Figs. S1–S7). The photodegradation study was performed using CV dye under visible-light irradiation. $Bi_{12}SiO_{20}$/20wt%-GO sample showed the best photocatalytic activity among all composite catalysts (Fig. S8), achieving 99% degradation of CV after 96 h of visible-light irradiation. The degradation rate constant over $Bi_{12}SiO_{20}$/20wt%-GO was 5.0×10^{-2} h^{-1}, which is 10 times more than the constant obtained over pure $Bi_{12}SiO_{20}$. Considering 2-hydroxybenzoic acid (2-HBA) as a target pollutant, about 66% of 2-HBA was photodegraded upon exposure to visible-light irradiation for 96 h with the $Bi_{12}SiO_{20}$/20wt%-GO composite. Fig. S9 shows the photocatalytic activity of the $Bi_{12}SiO_{20}$/20wt%-GO composite in repeated recycling experiments, which decreased to 36% degradation efficiency in the fifth run. In conclusion, $Bi_{12}SiO_{20}$/GO composites had reduced photocatalytic activity in degradation of CV and 2-HBA and were less stable in recycling experiments in comparison to $Bi_{12}SiO_{20}$/g-C_3N_4 photocatalysts.

3.4. Photodegradation mechanisms of CV

Scavenger experiments were performed to provide better understanding of the roles of the active species in this photodegradation process. Ammonium oxalate (AO), benzoquinone (BQ), isopropanol (IPA), and sodium azide (SA) were added as scavengers for the h^+, $\bullet O_2^-$, •OH, and $^1O_2$ potential active species, respectively [21]. The experimental results in the presence and absence of the four scavengers on the photocatalytic degradation of the CV dye with 5wt%-$Bi_{12}SiO_{20}$/g-C_3N_4 catalyst under visible-light irradiation are summarized in Fig. 11a. h^+ and $^1O_2$ species were found to have less important roles in the photocatalytic degradation of CV since negligible changes in the degradation efficiencies were observed upon adding AO and SA. In contrast, the introduction of the IPA and BQ scavengers had a noticeable inhibitory effect on the degradation process, inferring that •OH and $\bullet O_2^-$ radicals are the principal active species in the proposed decomposition of CV.

Next, ESR spin–trap technique (with DMPO) was employed to detect the reactive radicals. Fig. 11(b) and (c) show the absence of any ESR signal in the dark. However, the principal signals for DMPO-•OH (intensity ratio: 1:2:2:1) and DMPO-$\bullet O_2^-$ (intensity ratio: 1:1:1:1) spin adducts were detected in the reactions under visible-light irradiation [46]. The intensity of the signals gradually increased with the prolonged reaction time. Thus, it can be concluded that the photocatalysts are activated upon exposure to visible light, and •OH and $\bullet O_2^-$ active radicals are generated. In conclusion, the ESR and scavenger experiments indicate that •OH and $\bullet O_2^-$ radicals are the principal active species in the photodegradation of the CV using the herein reported composite material, whereas h^+ and $^1O_2$ have less important roles in the process.

A plausible mechanism that accounts for the high photocatalytic activity of the $Bi_{12}SiO_{20}$/g-C_3N_4 composite can be postulated based on the previous experiments Fig. 12). The electrons in the valence bands of g-C_3N_4 and $Bi_{12}SiO_{20}$ are excited to the respective conduction bands upon irradiating the composite with visible light, leaving holes (h^+) in the valence bands. The photoinduced electrons in the conduction band of g-C_3N_4 can transfer easily to the surface of $Bi_{12}SiO_{20}$, and the h^+ in the valence band of $Bi_{12}SiO_{20}$ can likewise transfer to the surface of g-C_3N_4. This transfer consequently decreases the possibility of electron-hole recombination. The production of reactive oxygen species, that are responsible for the CV decomposition, is induced once electrons reach the conduction band of $Bi_{12}SiO_{20}$. The photodegradation of CV can occur via a photosensitizing process mediated by $Bi_{12}SiO_{20}$/g-C_3N_4, in addition to another photocatalytic route, which enhances the photocatalytic activity. Fig. 12 shows that the photosensitization and photocatalysis processes are preceded simultaneously. The reaction between the photosensitized and photogenerated electrons and the oxygen on the surface of the semiconductor generates $\bullet O_2^-$ radicals. In turn, these oxygen species can further react with H^+ ions (and subsequently with electrons and water) to produce •OH radicals; Eqs. (6) – ((9). •OH radicals can also be produced by the reactions between photogenerated holes and OH^- ions or H_2O; Eqs. (10) and (11). These cycles occur continually upon irradiating the system by visible light [47], consequently leading to the photodegradation of CV dye (or 2-HBA)

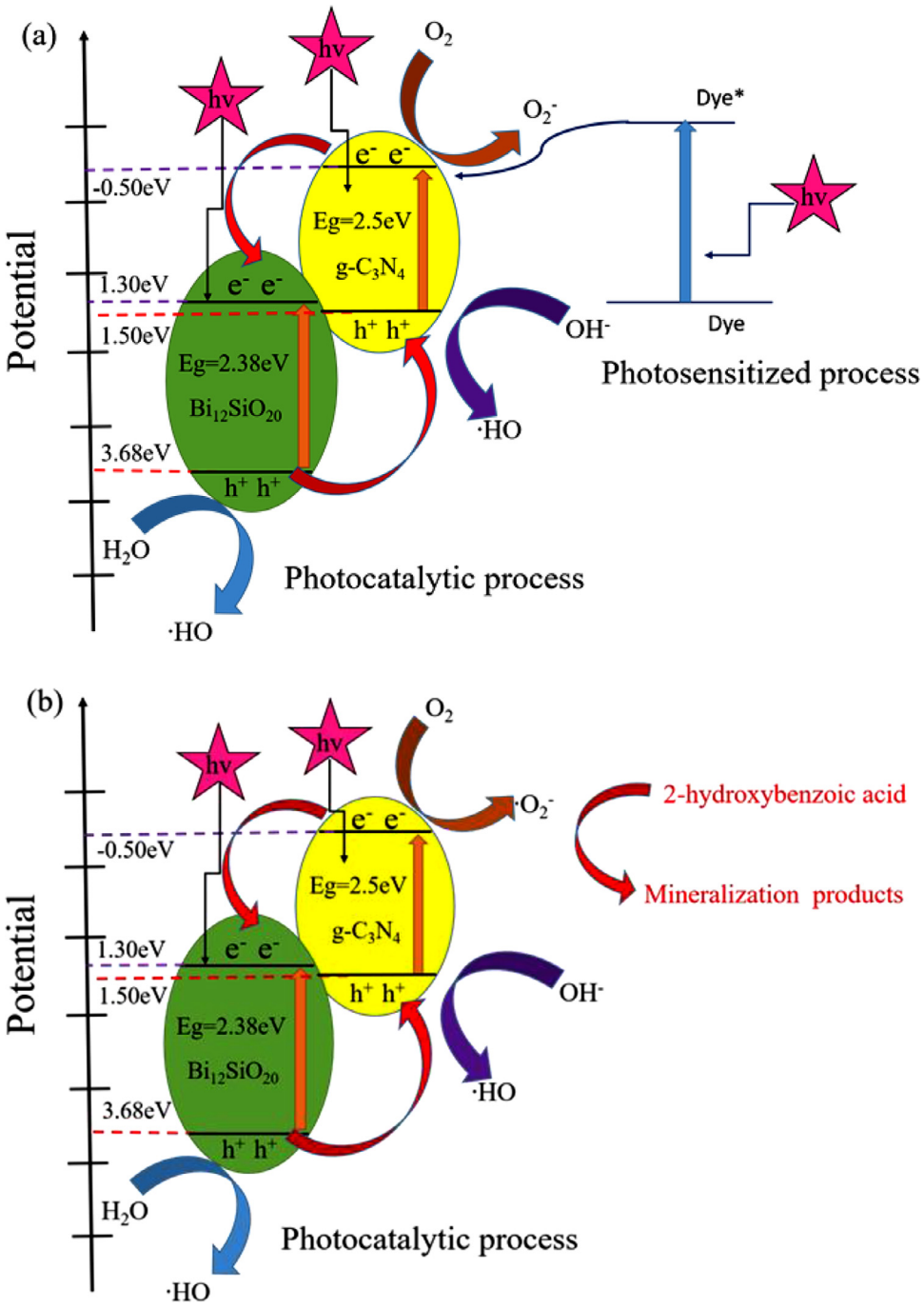

Fig. 12. The band structure diagram of $Bi_{12}SiO_{20}$/g-C_3N_4 and the possible charge separation processes: (a) CV degradation, (b) 2-HBA degradation.

by the active radical species ($\bullet O_2^-$ and •OH) after several cycles of photo-oxidation; Eqs. (12) and (13).

$$\bullet O_2^- + H^+ + e^- \rightarrow HOO^\bullet \quad (6)$$

$$HOO^\bullet + H_2O \rightarrow {}^\bullet OH + H_2O_2 \quad (7)$$

$$\bullet O_2^- + 2H^+ \rightarrow H_2O_2 \quad (8)$$

$$H_2O_2 + e^- \rightarrow {}^\bullet OH + OH^- \quad (9)$$

$$h^+ + OH^- \rightarrow {}^\bullet OH \quad (10)$$

$$h^+ + H_2O \rightarrow {}^\bullet OH + H^+ \quad (11)$$

$$CV(or 2-HBA) + \bullet O_2^-/{}^\bullet OH \rightarrow degraded compounds \quad (12)$$

$$CV^{+\bullet}(or 2-HBA) + \bullet O_2^-/{}^\bullet OH \rightarrow degraded compounds \quad (13)$$

Metal-organic frameworks (MOFs) have also been reported as efficient photocatalysts for degradation of dyes [48–51]. The photocatalytic mechanism of $Bi_{12}SiO_{20}$/g-C_3N_4 in the degradation of CV is similar to that of reported MOF-based catalysts and the reported composite materials herein had comparable photocatalytic activities using a visible light source.

The photocatalytic degradation mechanism of CV dye under UV or visible light has been reported to proceed by generating carbon-

centered radicals resulting in the cleavage of the conjugated molecule and nitrogen-centered radicals in *N*-dealkylation processes [52–54]. Additionally, hydroxylated products have also been detected in CV degradation using visible-light-induced semiconductor systems [47,55]. The proposed photocatalytic mechanisms using $Bi_{12}SiO_{20}$/g-C_3N_4 system in this work should provide some insight for this dye decolorization application.

4. Conclusions

In this work, a template-free hydrothermal method was used to synthesize new $Bi_{12}SiO_{20}$/g-C_3N_4 heterojunction for photocatalytic degradation applications of organic contaminants. The prepared materials were characterized by XRD, SEM-EDS, HRTEM, FT-IR, XPS, DRS, BET, PL, and EPR. The 5wt%-$Bi_{12}SiO_{20}$/g-C_3N_4 catalysts significantly enhanced the degradation efficiency of crystal violet in comparison to pristine $Bi_{12}SiO_{20}$ and g-C_3N_4. The optimal rate constant of the CV photocatalytic degradation with the $Bi_{12}SiO_{20}$/g-C_3N_4 composite was found to be 15 and 2 times greater than the constants obtained with $Bi_{12}SiO_{20}$ and g-C_3N_4 catalysts, respectively. $Bi_{12}SiO_{20}$/GO composites were synthesized to compare the $Bi_{12}SiO_{20}$/g-C_3N_4 heterojunction to other Bi composite materials, and were found to have reduced photocatalytic activity and stability in degradation of CV and 2-HBA. The 5wt%-$Bi_{12}SiO_{20}$/g-C_3N_4 composite material was further tested for the photocatalytic degradation of 2-HBA and RhB, yielding 98% and 99.5% degradation with visible-light irradiation for 72 h, respectively. The higher photocatalytic activities of the composite catalyst can be explained by formation of a heterojunction between $Bi_{12}SiO_{20}$ and g-C_3N_4, leading to efficient reduction of the recombination of photogenerated electron-hole pairs. Reactive •OH and $\bullet O_2^-$ radicals were found to be the major reactive species in the CV degradation. In conclusion, the $Bi_{12}SiO_{20}$/g-C_3N_4 composite demonstrated good photocatalytic activity, stability and reusability for photodegradation of organic compounds (CV, 2-HBA, and RhB) under visible-light irradiation. These results demonstrate the prospect of the $Bi_{12}SiO_{20}$/g-C_3N_4 heterojunction in photocatalytic degradation applications.

Declaration of Competing Interest

The authors declare that they have no known competing financial interests or personal relationships that could have appeared to influence the work reported in this paper.

Acknowledgments

This research was supported by the Ministry of Science and Technology of the Republic of China (MOST-109–2113-M-142–001).

Supplementary materials

Supplementary material associated with this article can be found, in the online version, at doi:10.1016/j.jtice.2021.05.042.

References

[1] Chen KT, Lu CS, Chang TH, Lai YY, Chang TH, Wu CW, Chen CC. Comparison of photodegradative efficiencies and mechanisms of Victoria Blue R assisted by Nafion-coated and fluorinated TiO_2 photocatalysts. J Hazard Mater 2010;174:598–609.
[2] Rajabi HR, Arjmand H, Kazemdehdashti H, Farsi M. A comparison investigation on photocatalytic activity performance and adsorption efficiency for the removal of cationic dye: quantum dots vs. magnetic nanoparticles. J Environ Chem Eng 2016;4:2830–40.
[3] Bayram E, Ayranci E. Investigation of changes in properties of activated carbon cloth upon polarization and of electrosorption of the dye basic blue-7. Carbon NY 2010;48:1718–30.
[4] Anirudhan TS, Divya PL, Nima J, Sandeep S. Synthesis and evaluation of iron-doped titania/silane based hydrogel for the adsorptional photocatalytic degradation of Victoria blue under visible light. J Coll Interface Sci 2014;434:48–58.
[5] Shamsipur M, Rajabi HR, Khani O. Pure and Fe^{3+}-doped ZnS quantum dots as novel and efficient nanophotocatalysts: synthesis, characterization and use for decolorization of Victoria blue R. Mater Sci Semicond Process 2013;16:1154–61.
[6] Huang S, Chen C, Tsai H, Shaya J, Lu C. Photocatalytic degradation of thiobencarb by a visible light-driven MoS_2 photocatalyst. Sep Purif Technol 2018;197:147–55.
[7] Chen CC, Shaya J, Fan HJ, Chang YK, Chi HT, Lu CS. Silver vanadium oxide materials: controlled synthesis by hydrothermal method and efficient photocatalytic degradation of atrazine and CV dye. Sep Purif Technol 2018;206:226–38.
[8] Chen F, Fang P, Gao Y, Liu Z, Liu Y, Dai Y. Effective removal of high-chroma crystal violet over TiO_2-based nanosheet by adsorption–photocatalytic degradation. Chem Eng J 2012;204–206:107–13.
[9] Ameen S, Akhtar MS, Nazim M, Shin HS. Rapid photocatalytic degradation of crystal violet dye over ZnO flower nanomaterials. Mater Lett 2013;96:228–32.
[10] Lee WW, Huang ST, Chang JL, Chen JY, Cheng MC, Chen CC. Photodegradation of CV over nanocrystalline bismuth tungstate prepared by hydrothermal synthesis. J Mol Catal A Chem 2012;361-362:80–90.
[11] Lee WW, Chung WH, Huang WS, Lin WC, Lin WY, Jiang YR, Chen CC. Photocatalytic activity and mechanism of nano-cubic barium titanate prepared by a hydrothermal method. J Taiwan Inst Chem Eng 2013;44:660–9.
[12] Yu K, Yang S, Liu C, Chen H, Li H, Sun C, Boyd SA. Degradation of organic dyes via bismuth silver oxide initiated direct oxidation coupled with sodium bismuthate based visible light photocatalysis. Environ Sci Technol 2012;46:7318–26.
[13] Meng A, Zhang L, Cheng B, Yu J. Dual cocatalysts in TiO_2 photocatalysis. Adv Mater 2019;31:e1807660.
[14] Feng W, Fang J, Zhang L, Lu S, Wu S, Cheng C, Chen Y, Ling Y, Fang Z. Plasmonic metallic Bi deposited $Bi_{12}SiO_{20}$ crystals with rich oxygen vacancies for enhanced photocatalytic degradation of RhB and 2,4-DCP. Mater Res Bull 2017;94:45–53.
[15] Han Q, Zhang J, Wang X, Zhu J. Preparing $Bi_{12}SiO_{20}$ crystals at low temperature through nontopotactic solid-state transformation and improving its photocatalytic activity by etching. J Mater Chem A 2015;3:7413–21.
[16] He C, Gu M. Preparation, characterization and photocatalytic properties of $Bi_{12}SiO_{20}$ powders. Scr Mater 2006;55:481–4.
[17] Wu Y, Lu J, Li M, Yuan J, Wu P, Chang X, Liu C, Wang X. Bismuth silicate photocatalysts with enhanced light harvesting efficiency by photonic crystal. J Alloy Compd 2019;810:151839.
[18] Deng F, Lu X, Zhao L, Luo Y, Pei X, Luo X, Luo S. Facile low-temperature co-precipitation method to synthesize hierarchical network-like g-C_3N_4/$SnIn_4S_8$ with superior photocatalytic performance. J Mater Sci 2016;51:6998–7007.
[19] Chen W, Liu TY, Huang T, Liu XH, Zhu JW, Duan GR, Yang XJ. One-pot hydrothermal route to synthesize the $ZnIn_2S_4$/g-C_3N_4 composites with enhanced photocatalytic activity. J Mater Sci 2015;50:8142–52.
[20] Wen J, Xie J, Chen X, Li X. A review on g-C_3N_4-based photocatalysts. Appl Surf Sci 2017;391:72–123.
[21] Lin HP, Chen CC, Lee WW, Lai YY, Chen JY, Chen YQ, Fu JY. Synthesis of $SrFeO_{3-x}$/g-C_3N_4 heterojunction with improved visible-light photocatalytic activities in chloramphenicol and crystal violet degradation. RSC Adv 2016;6:2323–36.
[22] Wang S, Li D, Sun C, Yang S, Guan Y, He H. Synthesis and characterization of g-C_3N_4/Ag_3VO_4 composites withsignificantly enhanced visible-light photocatalytic activity fortriphenylmethane dye degradation. Appl Catal B Environ 2014;144:885–92.
[23] Chen X, He X, Yang X, Wu Z, Li Y. Construction of novel 2D/1D g-C_3N_4/$CaTiO_3$ heterojunction with face-to-face contact for boosting photodegradation of triphenylmethane dyes under simulated sunlight. J Taiwan Inst Chem Eng 2020;107:98–109.
[24] Manimozhi R, Mathankumar M, Gnana Prakash AP. Synthesis of g-C_3N_4/ZnO heterostructure photocatalyst for enhanced visible degradation of organic dye. Optik 2021;229:165548 (Stuttg).
[25] Zhu K, Lv Y, Liu J, Wang W, Wang C, Li S, Wang P, Zhang M, Meng A, Li Z. Facile fabrication of g-C_3N_4/SnO_2 composites and ball milling treatment for enhanced photocatalytic performance. J Alloy Compd 2019;802:13–8.
[26] Devarayapalli KC, Prabhakar SVV, Sreekanth TVM, Yoo KS, Nagajyothi PC, Shim J. Hydrogen production and photocatalytic activity of g-C_3N_4/Co-MOF (ZIF-67) nanocomposite under visible light irradiation. Appl Organomet Chem 2020;34:e5376.
[27] Prakash K, Karuthapandian S, Senthilkumar S. Zeolite nanorods decorated g-C_3N_4 nanosheets: a novel platform for the photodegradation of hazardous water contaminants. Mater Chem Phys 2019;221:34–46.
[28] Lu P, Hu X, Li Y, Peng Y, Zhang M, Jiang X, He Y, Fu M, Dong F, Zhang Z. Novel $CaCO_3$/g-C_3N_4 composites with enhanced charge separation and photocatalytic activity. J Saudi Chem Soc 2019;23:1109–18.
[29] Zhang JY, Zhang SH, Li J, Zheng XC, Guan XX. Constructing of 3D graphene aerogel-g-C_3N_4 metal-free heterojunctions with superior purification efficiency for organic dyes. J Mol Liq 2020;310:113242.
[30] Chen W, Huang T, Hua YX, Liu TY, Liu XH, Chen SM. Hierarchical $CdIn_2S_4$ microspheres wrapped by mesoporous g-C_3N_4 ultrathin nanosheets with enhanced visible light driven photocatalytic reduction activity. J Hazard Mater 2016;320:529–38.
[31] Li WQ, Wen ZH, Tian SH, Shan LJ, Xiong Y. Citric acid-assisted hydrothermal synthesis of a self-modified Bi_2SiO_5/$Bi_{12}SiO_{20}$ heterojunction for efficient photocatalytic degradation of aqueous pollutants. Catal Sci Technol 2018;8:1051–61.
[32] Yang CT, Lee WW, Lin HP, Dai YM, Chi HT, Chen CC. A novel heterojunction photocatalyst, Bi_2SiO_5/g-C_3N_4: synthesis, characterization, photocatalytic activity, and mechanism. RSC Adv 2016;6:40664–75.

[33] Wang S, Li D, Sun C, Yang S, Guan Y, He H. Synthesis and characterization of g-C_3N_4/Ag_3VO_4 composites with significantly enhanced visible-light photocatalytic activity for triphenylmethane dye degradation. Appl Catal B Environ 2014;144:885–92.
[34] Chen CC, Yang CT, Chung WH, Chang JL, Lin WY. Synthesis and characterization of $Bi_4Si_3O_{12}$, Bi_2SiO_5, and $Bi_{12}SiO_{20}$ by controlled hydrothermal method and their photocatalytic activity. J Taiwan Inst Chem Eng 2017;78:157–67.
[35] Wu SZ, Li K, Zhang WD. On the heterostructured photocatalysts Ag_3VO_4/g-C_3N_4 with enhanced visible light photocatalytic activity. Appl Surf Sci 2015;324:324–31.
[36] Lu YC, Chen CC, Lu CS. Photocatalytic degradation of bis(2-chloroethoxy)methane by a visible light-driven $BiVO_4$ photocatalyst. J Taiwan Inst Chem Eng 2014;45:1015–24.
[37] Jiang D, Li J, Xing C, Zhang Z, Meng S, Chen M. Two-dimensional $CaIn_2S_4$/g-C_3N_4 heterojunction nanocomposite with enhanced visible-light photocatalytic activities: interfacial engineering and mechanism insight. ACS Appl Mater Interface 2015;7:19234–42.
[38] Li H, Liu J, Hou W, Du N, Zhang R, Tao X. Synthesis and characterization of g-C_3N_4/Bi_2MoO_6 heterojunctions with enhanced visible light photocatalytic activity. Appl Catal B Environ 2014;160-161:89–97.
[39] Hu W, Yu J, Jiang X, Liu X, Jin R, Lu Y, Zhao L, Wu Y, He Y. Enhanced photocatalytic activity of g-C_3N_4 via modification of $NiMoO_4$ nanorods. Coll Surf A Physicochem Eng Asp 2017;514:98–106.
[40] Zhao L, Zhang L, Lin H, Nong Q, Cui M, Wu Y, He Y. Fabrication and characterization of hollow $CdMoO_4$ coupled g-C_3N_4 heterojunction with enhanced photocatalytic activity. J Hazard Mater 2015;299:333–42.
[41] Xiao K, Huang H, Tian N, Zhang Y. Mixed-calcination synthesis of Bi_2MoO_6/g-C_3N_4 heterojunction with enhanced visible-light-responsive photoreactivity for RhB degradation and photocurrent generation. Mater Res Bull 2016;83:172–8.
[42] Ou M, Zhong Q, Zhang S, Yu L. Ultrasound assisted synthesis of heterogeneous g-C_3N_4/$BiVO_4$ composites and their visible-light-induced photocatalytic oxidation of NO in gas phase. J Alloy Compd. 2015;626:401–9.
[43] Guo F, Shi W, Lin X, Che G. Hydrothermal synthesis of graphitic carbon nitride–$BiVO_4$ composites with enhanced visible light photocatalytic activities and the mechanism study. J Phys Chem Solid 2014;75:1217–22.
[44] Lu X, Wang Y, Zhang X, Xu G, Wang D, Lv J, Zheng Z, Wu Y. NiS and MoS_2 nanosheet co-modified graphitic C_3N_4 ternary heterostructure for high efficient visible light photodegradation of antibiotic. J Hazard Mater 2018;341:10–9.
[45] Tsai H, Shaya J, Tesana S, Golovko VB, Wang SY, Liao YY, Lu CS, Chen CC. Visible-light driven photocatalytic degradation of pirimicarb by Pt-doped $AgInS_2$ nanoparticles. Catalysts 2020;10:857.
[46] Chen CC, Fan HJ, Shaya J, Chang YK, Golovko VB, Toulemonde O, Huang CH, Song YX, Lu CS. Accelerated $ZnMoO_4$ photocatalytic degradation of pirimicarb under UV light mediated by peroxymonosulfate. Appl Organomet Chem 2019;33:e5113.
[47] Wendell WD, Yosihiro A, Allen JB. Characterization of particulate titanium dioxide photocatalysts by photoelectrophoretic and electrochemical measurements. J Am Chem Soc 1981;103:3456–9.
[48] Wang J, Rao C, Lu L, Zhang S, Muddassir M, Liu J. Efficient photocatalytic degradation of methyl violet using two new 3D MOFs directed by different carboxylate spacers. Crystengcomm 2021;23:741–7.
[49] Liu KG, Rouhani F, Gao XM, Abbasi-Azad M, Li JZ, Hu XD, Wang W, Hu ML, Morsali A. Bilateral photocatalytic mechanism of dye degradation by a target designed ferrocene-functionalized cluster under natural sunlight. Catal Sci Technol 2020;10:757–67.
[50] Jin JC, Wu J, Liu WC, Ma AQ, Liu JQ, Singh A, Kumar A. A new Zn(II) metal-organic framework having 3D $CdSO_4$ topology as luminescent sensor and photocatalyst for degradation of organic dyes. New J Chem 2018;42:2767–75.
[51] Hu ML, Safarifard V, Doustkhah E, Rostamnia S, Morsali A, Nouruzi N, Beheshti S, Akhbari K. Taking organic reactions over metal-organic frameworks as heterogeneous catalysis. Microporous Mesoporous Mater 2018;256:111–27.
[52] Fan HJ, Lu CS, Lee WL, Chiou MR, Chen CC. Mechanistic pathways differences between P25-TiO_2 and Pt-TiO_2 mediated CV photodegradation. J Hazard Mater 2011;185:227–35.
[53] Li Y, Yang S, Sun C, Wang L, Wang Q. Aqueous photofate of crystal violet under simulated and natural solar irradiation: kinetics, products, and pathways. Water Res 2016;88:173–83.
[54] Li X, Liu G, Zhao J. Two competitive primary processes in the photodegradation of cationic triarylmethane dyes under visible irradiation in TiO_2 dispersions. New J Chem 1999;23:1193–6.
[55] Lee WW, Lu CS, Chuang CW, Chen YJ, Fu JY, Siao CW, Chen CC. Synthesis of bismuth oxyiodides and their composites: characterization, photocatalytic activity, and degradation mechanisms. RSC Adv 2015;5:23450–63.